



# Influence of the electrolyte film thickness and NaCl concentration on the oxygen reduction current on platinum



O. Dolgikh<sup>a,\*</sup>, A.C. Bastos<sup>b</sup>, A. Oliveira<sup>b</sup>, C. Dan<sup>a</sup>, J. Deconinck<sup>a</sup>

<sup>a</sup> Research Group SURF, Vrije Universiteit Brussel, Pleinlaan 2, 1050 Brussels, Belgium

<sup>b</sup> DEMaC/CICECO, Universidade de Aveiro, Campus Universitário de Santiago, 3810-193 Aveiro, Portugal

## ARTICLE INFO

### Article history:

Received 14 April 2015

Received in revised form 16 October 2015

Accepted 17 October 2015

Available online 28 October 2015

### Keywords:

Platinum

Potentiostatic

Modelling studies

Oxygen reduction

## ABSTRACT

Measurements of oxygen reduction current are performed on a platinum electrode submerged under NaCl electrolyte films of different thickness. The chloride concentration is kept constant or increases due to evaporation. Measurements are supported by the numerical Multi-Ion Transport and Reaction Model (MITReM). In case of constant salt concentration, oxygen reduction current is proportional to the reciprocal of the electrolyte film thicknesses down to 50–75 μm; for lower thicknesses deviation from the Fick's law takes place. For evaporating films, oxygen current is the result of two counteracting phenomena: reducing film thickness and increasing salt concentration leading to decrease of oxygen solubility.

© 2015 Elsevier Ltd. All rights reserved.

## 1. Introduction

According to the electrochemical theory of metal corrosion introduced by N.D. Tomashov in 1960s [1], oxygen reduction determines the corrosion rate of many metals under electrolyte films with a thickness above 1 μm. Oxygen reduction, in turn, is controlled by the dissolution rate of oxygen from the air and mass-transport of the dissolved gas from the electrolyte/air interface towards the electrode surface. As a consequence, the rate of this reaction depends substantially on the electrolyte film thickness and on the O<sub>2</sub> solubility that is influenced by electrolyte nature and concentration. This factor becomes especially relevant during a corrosion process where an accumulation of metal and hydroxide ions takes place and leads to substantial changes in the electrolyte composition. Moreover, if a corrosion process occurs in wet/dry conditions, concentration changes due to the evaporation/condensation of liquid can be even more significant. That is why knowledge of the influence of the electrolyte films thickness and composition on the oxygen reduction rate is very important.

In the literature a number of publications are devoted to the measurements of corrosion rates of different metals covered by thin electrolyte films (including films with changing in time

thickness) [2–11] or droplets [12]. The measurements cover electrolyte films thicknesses ranging from millimeters down to a few micrometers and are performed using different techniques: Kelvin probe [3,4], electrochemical impedance [5–8], linear voltammetry [9–12]. The lower limit of film thicknesses depends on the applied measuring technique, as in very thin layers the problem of electrical contact between electrodes arises. Another restriction is the possibility of creating, measuring and maintaining the continuous electrolyte film on the electrode surface during the measurements, especially if the corrosion process involves the formation of precipitates. When summarizing the published experimental data, one can conclude that in neutral electrolytes oxygen reduction current is almost independent on the electrolyte film thickness  $\delta_F$  when  $\delta_F > (0.5–1)$  mm [2–4,8–10]. With further decrease of the layer thickness the reduction rate increases proportionally to  $1/\delta_F$ . Several authors report the lower limit of such an increase at about 10–30 μm [7,9,11,13]. Below these thicknesses, the oxygen current density either decreases [3,11], or remains constant depending on the metal and electrolyte nature [9].

Another way to study the role of different factors in oxygen reduction is modeling. Despite the number of publications on corrosion modeling in immersed conditions, only few simulation examples, to the best of our knowledge, has been performed for thin electrolyte layers. Venkatraman et al. [14] have presented a 1D mathematical model for the free corrosion of a bare metal surface under electrolyte layers of different thickness using the mixed potential theory. This model assumed a pseudo-steady state where the oxygen diffusion was in a stationary regime while metal and

\* Corresponding author.

E-mail addresses: [Olga.Dolgikh@vub.ac.be](mailto:Olga.Dolgikh@vub.ac.be) (O. Dolgikh), [acbastos@ua.pt](mailto:acbastos@ua.pt) (A.C. Bastos), [arboliveira@ua.pt](mailto:arboliveira@ua.pt) (A. Oliveira), [calin.dan@vub.ac.be](mailto:calin.dan@vub.ac.be) (C. Dan), [Johan.Deconinck@vub.ac.be](mailto:Johan.Deconinck@vub.ac.be) (J. Deconinck).

hydroxyl ions are accumulating. Palani et al. [15] validated a predictive numerical model for galvanic corrosion under thin electrolyte layers that is based on the Laplace's equation and provides current and potential distributions along the electrode surface. Thébault et al. [16] have developed a more elaborated two-dimensional finite element model for galvanic corrosion studies solving the Laplace's equation for potential together with the second Fick's law for oxygen transport. The outcome of the model was in agreement with the literature data. However, it provides a stationary potential distribution for an electrolyte of given conductivity and does not take into account possible changes of the electrolyte conductivity and/or oxygen solubility during the corrosion process.

In this article, we present the results of an experimental and modeling study on the oxygen reduction reaction on a platinum electrode covered by NaCl electrolyte layers of different thickness. Measurements are performed for three salt concentrations (5, 50 and 500 mM) and for electrolyte layers that are kept at constant thickness and that change in time due to evaporation. Platinum is chosen because it is stable in chloride electrolytes at the applied potentials. In addition, it gives the possibility to study the oxygen reduction process without possible formation of precipitating corrosion products. Based on dedicated experimental input, the time-dependent numerical Multi-Ion Transport and Reaction Model (MITReM) is developed in order to describe and predict the oxygen reduction currents for the studied conditions.

## 2. Experimental

### 2.1. Measurements of oxygen solubility

The measurements of the oxygen solubility were performed by an amperometric technique in the bulk of NaCl solutions of varying concentration, with a 3 mm diameter platinum disk electrode rotating at 100 rpm, polarized at  $-0.75$  V with respect to a low leakage Ag|AgCl|3M KCl reference electrode (DRIREF2, World Precision Instruments, USA) and using a platinum counter electrode. At this potential the dissolved oxygen is being reduced under diffusion control, and the concentration of  $O_2$  can be obtained using the Levich equation

$$c_{O_2} = \frac{I_{lim}}{0.62nFAD^{2/3}\nu^{-1/6}\omega^{1/2}}, \quad (1)$$

where  $I_{lim}$  is the limiting current of oxygen reduction,  $n=4$  is the number of electrons,  $F$  is Faraday's constant,  $D = 1.96 \times 10^{-9} \text{ m}^2\text{s}^{-1}$  is the oxygen diffusion coefficient [17],  $A$  is the electrode area,  $\nu$  is the kinematic viscosity of the solution that varied in the interval  $(9.0-14.5) \times 10^{-7} \text{ m}^2\text{s}^{-1}$  depending on the solution concentration [18], and  $\omega = 2\pi f$  is the angular frequency of rotation with  $f$  being the frequency in Hz.

Air was bubbled through the electrolyte for 10 min prior to the measurements in order to saturate it with oxygen. The solution temperature was  $24.5 \pm 0.5^\circ\text{C}$  during bubbling and measurements.

### 2.2. Electrochemical cell and measurements of the electrolyte film thickness

Measurements were performed in the specially designed electrochemical cell schematically shown in Fig. 1. The working electrode was a platinum strip ( $0.95 \times 10 \text{ mm}^2$ ) embedded in epoxy resin. The counter electrode of a large area made of a Pt wire was placed in a recess next to the working electrode at a distance of 2–3 mm. The shape and the position of the counter electrode were chosen in a such way that the potential distribution in the recess is uniform (for confirmation see Section 4.2). The reference electrode was Ag/AgCl wire inside a glass pipette filled with agar-agar gel made with the same solution as the one used for the measurements. The potentials of the electrodes containing 5, 50 and 500 mM NaCl as internal solution were respectively, 110 mV, 63 mV and 12 mV with respect to the saturated calomel electrode. The electrode tip was placed inside the recess in order to avoid drying, prevent loss of the electrical contact and also to prevent the effect of a solution meniscus close to the working electrode. The thickness of the electrolyte layer above the working electrode was measured using a video camera coupled to a lens and a sharp needle in a 3D stepper motor positioning system with  $1 \mu\text{m}$  accuracy. After touching the surface of the electrode (zero height) the needle was moved out of solution. When approaching back, a meniscus was formed once the needle touched the liquid surface. This height corresponded to the thickness of the solution layer.

### 2.3. Measurements of polarization curves and current transients

Polarization curves were recorded by changing the potential of the working electrode in cathodic direction with a scan rate of  $1 \text{ mV s}^{-1}$  starting from a potential  $\sim 100 \text{ mV}$  more positive than the

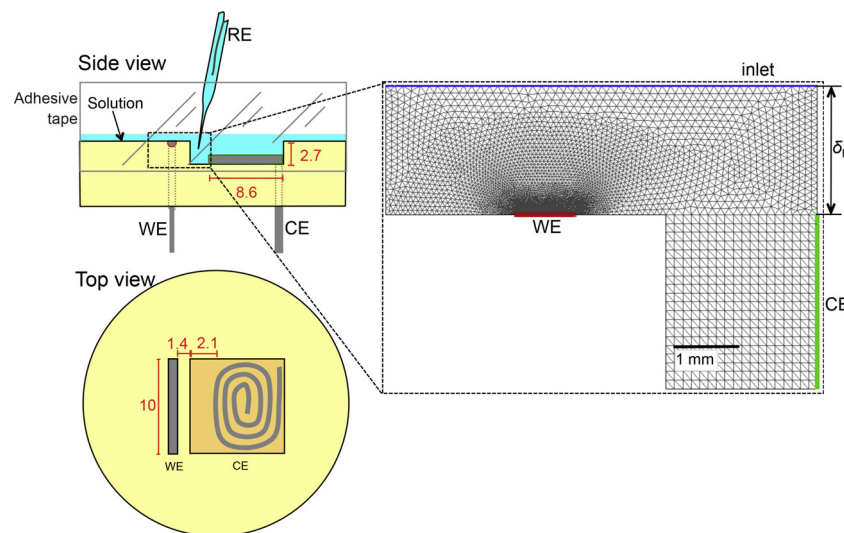


**Fig. 1.** Schematics of the electrochemical cell used for the measurements and discretization of the computational domain (WE, working electrode; CE, counter electrode; RE, reference electrode;  $\delta_F$ , the thickness of the electrolyte layer). All dimensions are given in millimeters.

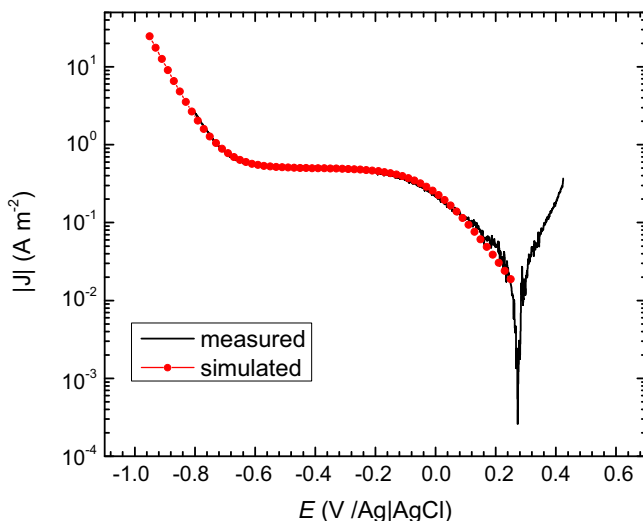


**Fig. 2.** Experimental and simulated polarization curves for Pt electrode in 50 mM NaCl solution (pH 5.5). Electrolyte film thickness 2 mm.

open circuit potential. A typical polarization curve recorded in the immersed conditions ( $\delta_F > 2$  mm) is shown in Fig. 2.

To obtain the current transients, the working electrode was polarized at  $-0.8/-0.7$  V vs. Ag|AgCl|5, 50 or 500 mM NaCl (depending on the test solution), potentials well inside the region of diffusion control of the oxygen reduction for each solution and thickness tested.

#### 2.4. Measurements of pH maps

pH maps in the plane perpendicular to the surface were obtained for the electrolyte thicknesses of 100 and 2000  $\mu\text{m}$ . The pH micro-potentiometric electrodes were made in the laboratory and consisted of borosilicate glass capillaries of 1.5 mm outer diameter thinned to a 2  $\mu\text{m}$  tip on one end, with a Ag|AgCl wire as internal reference, a filling solution of 0.1 M KCl +  $\text{KH}_2\text{PO}_4$  0.01 M and a 20–30  $\mu\text{m}$  column of hydrogen I cocktail B ionophore at the tip (Fluka, Ref. 95293).

The microelectrode was inserted in a pre-amplifier, which was mounted in a 3D positioning system and connected to an IPA2 amplifier (both from Applicable Electronics Inc., USA). The microelectrodes were calibrated before and after measurements with commercial pH buffers (Riedel-de Haen), giving a linear response in the 5–13 pH range. More details can be found in Ref. [19].

### 3. Modeling

In order to describe the phenomena that take place during cathodic polarization of platinum electrode in aqueous NaCl electrolytes (pH 5.5), a Multi-Ion Transport and Reaction Model (MITReM) was developed. The model takes into account transport of all relevant species in the electrolyte, their production/consumption at the electrode and the air/electrolyte interface and homogeneous reactions. The Finite Element Method (FEM) is used to solve the balance equations for the concentration of dissolved species  $c_k$  and the electrolyte potential  $U$ .

#### 3.1. Governing equations

The first set of the MITReM governing equations is the mass balances of each individual species  $k$ :

$$\frac{\partial c_k}{\partial t} = -\vec{\nabla} \cdot \vec{N}_k + R_k, \quad (2)$$

where  $\vec{N}_k$  ( $\text{mol m}^{-2} \text{s}^{-1}$ ) is the molar flux of species  $k$  with concentration  $c_k$  ( $\text{mol m}^{-3}$ ) and

$$R_k = \sum_{r=1}^R v_r s_{kr} \quad (3)$$

is the production term due to chemical reactions ( $v_r$  the rate of chemical reaction  $r$  and  $s_{kr}$  the stoichiometric coefficient of species  $k$  in the reaction  $r$ ).

The second governing equation required for the calculation of the solution potential is the electroneutrality condition:

$$\sum_{k=1}^K z_k c_k = 0. \quad (4)$$

The molar flux is the sum of contributions of convection, diffusion and migration

$$\vec{N}_k = c_k \vec{v} - D_k \vec{\nabla} c_k - \frac{z_k F D_k c_k}{RT} \vec{\nabla} U \quad (5)$$

with  $\vec{v}$  the solvent velocity ( $\text{m s}^{-1}$ );  $D_k$  ( $\text{m}^2 \text{s}^{-1}$ ) and  $z_k$  the diffusion coefficient and charge number of species  $k$  respectively;  $U$  (V) the solution potential;  $T$  (K) the temperature;  $F$  Faraday's constant and  $R$  universal gas constant.

For stagnant electrolytes, it is often assumed that the solvent velocity  $\vec{v} = 0$ . However this assumption leads in simulations to the unrealistic situation where diffusion and migration extend throughout the electrolyte layer thickness. In practice always a small but uncontrolled and unknown flow is created by the local microscopic motion of species due to the temperature gradients, evaporation, vibrations etc. (so-called micro-convection). This motion leads after some time to the establishment of an effective diffusion boundary layer. Based on the seminal work of Levich [20], Amatore et al. [21] were the first who introduced this idea for a single species problem and showed that the micro-convection contribution can be described by a diffusion-like term  $-D_{\mu\text{conv}} \vec{\nabla} c$ . In a separate paper we extended their ideas for the multi-ion systems [22] and showed that with use of micro-convection, the flux of species (Eq. (5)) can be rewritten as:

$$\vec{N}_k = -(D_k + D_{\mu\text{conv}}^{\text{ref}}) \vec{\nabla} c_k - \frac{z_k F D_k c_k}{RT} \vec{\nabla} U. \quad (6)$$

The coefficient  $D_{\mu\text{conv}}^{\text{ref}}$  is independent on the nature of the species  $k$ , and depends only on the distance from the wall (electrode)  $l$ :

$$D_{\mu\text{conv}}^{\text{ref}} = 1.5072 \cdot D^{\text{ref}} \left( \frac{l}{\Lambda^{\text{ref}}} \right)^4, \quad (7)$$

where  $D^{\text{ref}}$  is a constant having units of a diffusion coefficient, and  $\Lambda^{\text{ref}}$  (m) is a distance scaling parameter. Eq. (7) shows that for wall distances  $l$  that are larger than  $\Lambda^{\text{ref}}$ , micro convection rapidly becomes dominant.

#### 3.2. Geometry and discretization

Due to its high aspect ratio, the electrochemical cell used for the measurements can be approximated by a two-dimensional computational domain (Fig. 1) where the *working electrode* is placed on the bottom of the left side and the *counter electrode* is represented by the right boundary. The top boundary is *inlet* permeable only for oxygen. Other boundaries are considered insulating. For FEM calculation, this geometry is discretized in 5000–13,500 nodes (11,000–25,000 triangle elements) depending on the electrolyte film thickness  $\delta_F$  with the refining around working electrode where the concentration and potential gradients are the highest (Fig. 1).

### 3.3. Calculation of the boundary displacement

For simulations of the evaporation process, mesh deformation calculations were performed in parallel with the MITReM calculations. The bottom of the geometry remained fixed and the top boundary (inlet) was moving down with a constant velocity  $v_g$ , different for different concentrations of salt. At each time step  $\Delta t$  the geometry was adapted using the level set method [23] and the elastic body analogy [24]. The solution fields were recalculated on each changed geometry.

### 3.4. Boundary conditions

At the electrolyte-air interface (inlet) the normal flux of oxygen is given by:

$$\frac{\partial c_{O_2}}{\partial n} = F_{O_2}^{\max} \left( 1 - \frac{c_{O_2}}{c_{O_2}^{\text{sat}}} \right) \quad (8)$$

with  $c_{O_2}$  the local oxygen concentration,  $c_{O_2}^{\text{sat}}$  the oxygen solubility in NaCl that depends, at constant pressure and temperature, on the chloride concentration, and  $F_{O_2}^{\max} = (2.6\text{--}4.5) \times 10^{-5} \text{ mol m}^{-2} \text{ s}^{-1}$  the maximum dissolution rate of oxygen at 25 °C [25]. Variation of  $F_{O_2}^{\max}$  in the mentioned range would result in the corresponding change of simulated current densities. Since no indication was found whether this parameter depends on the electrolyte thickness or chloride concentration, an average value of  $F_{O_2}^{\max} = 3.5 \times 10^{-5} \text{ mol m}^{-2} \text{ s}^{-1}$  was used for all simulations.

At the counter electrode, all species bulk concentrations and a fixed electrolyte potential are imposed making it a virtual electrode:

$$c_k = c_k^{\text{bulk}}, \quad U = 0. \quad (9)$$

At the working electrode, the fluxes normal to the electrode surface are given by the rates of the electrochemical reactions:

$$\vec{N}_k \cdot \vec{I}_n = - \sum_{e=1}^E v_e s_{ke}, \quad (10)$$

where  $v_e$  is the rate of an electrode reaction  $e$  and  $s_{ke}$  is the stoichiometric coefficient of species  $k$  in this reaction. In this work, electrode reactions are considered as irreversible and their rates are given by the Tafel equation:

$$v_e = -k_{\text{red}} \exp \left[ -\frac{nF\alpha_{\text{red}}}{RT} (V - U) \right] c_{\text{Ox}} \quad (11)$$

with  $n$  number of electrons involved in the electrochemical reaction,  $k_{\text{red}}$  and  $\alpha_{\text{red}}$  rate constants and charge transfer coefficients respectively,  $V$  (V), the electrode potential and  $c_{\text{Ox}}$  the local concentration of oxidants. The total current density is the sum of all partial currents of the individual electrochemical reactions taking place at the working electrode

$$J_{\text{tot}} = \sum_{e=1}^E J_e = F \sum_{e=1}^E n_e v_e. \quad (12)$$

At the insulating walls, normal flux of species and potential gradients are set to zero:

$$\vec{N}_k \cdot \vec{I}_n = 0, \quad \frac{\partial U}{\partial n} = 0. \quad (13)$$

### 3.5. Electrolyte species, electrode and chemical reactions

The species considered in the model are the electrolyte ions ( $\text{Na}^+$ ,  $\text{Cl}^-$ ,  $\text{H}^+$  and  $\text{OH}^-$ ) and the dissolved molecular oxygen  $\text{O}_2$ .

**Table 1**

Species considered in the model with their charges, diffusivities and bulk concentrations.

Species	$z_k$	$D_k \times 10^9, \text{ m}^2 \text{ s}^{-1}$	$c_k^{\text{bulk}}, \text{ mol m}^{-3}$
$\text{Na}^+$	+1	1.23/1.22/1.00*	5/50/500
$\text{Cl}^-$	-1	1.82/1.80/1.21*	5/50/500
$\text{H}^+$	+1	9.31 [41]	$3.16 \times 10^{-3}$
$\text{OH}^-$	-1	5.26 [41]	$3.16 \times 10^{-6}$
$\text{O}_2$	0	1.96 [17]	0.249/0.245/0.208*

\* Different values of a parameter correspond to the different concentrations of NaCl.

Initial (bulk) concentrations of the species together with their charge numbers and diffusion coefficients are listed in Table 1.

Remark that the diffusion coefficients for  $\text{Na}^+$  and  $\text{Cl}^-$  were adjusted for each NaCl concentration in order to match the measured electrolyte conductivity ( $5.8 \times 10^{-2}$ ,  $5.75 \times 10^{-1}$  and  $4.2 \text{ S m}^{-1}$  for 5, 50 and 500 mM NaCl solutions respectively).

It is widely accepted in the literature (see e.g. [26–29]) that on platinum, oxygen reduction to water can follow two parallel paths: direct four-electron transfer and two consecutive two-electron transfers with  $\text{H}_2\text{O}_2$  as an intermediate. The amount of  $\text{H}_2\text{O}_2$  formed is greater in alkaline media but even there a contribution of two-electron reaction to the total current does not exceed 20% [27]. In the present model, only four-electron reaction (Eq. (14)) is taken into account. The second electrochemical reaction considered here is the hydrogen evolution from water molecules (Eq. (15)). Both reactions are assumed to be irreversible:



The kinetic parameters of these reactions ( $k_{\text{red}}$  and  $\alpha_{\text{red}}$ ) are first estimated by fitting in the classical way the experimental polarization curve (Fig. 2) to the Tafel equations (11). Final tuning of the kinetic parameters together with the value of the parameter  $\Lambda^{\text{ref}}$  is done by performing full MITReM simulations and comparing thus obtained polarization curve with the measured one.

For practical reasons oxygen is chosen as a reference species for the micro-convection term such that  $D_{\mu\text{conv}}^{\text{ref}} = 2.0 \times 10^{-9} \text{ m}^2 \text{ s}^{-1}$ . It was found that the parameters of the measured polarization curves are independent on chloride concentration. The best agreement with the measurements gives the following set of parameters:  $k(\text{O}_2) = 2.5 \times 10^{-6} \text{ s}^{-1}$ ,  $\alpha(\text{O}_2) = 0.15$ ;  $k(\text{H}_2\text{O}) = 1.0 \times 10^{-11} \text{ s}^{-1}$ ,  $\alpha(\text{H}_2\text{O}) = 0.175$ ,  $\Lambda^{\text{ref}} = 1.2 \times 10^{-3} \text{ m}$ . These parameters, though obtained for immersed conditions, are used for simulations at all investigated electrolyte thicknesses.

The only chemical reaction considered in the model is the water dissociation ( $\text{H}_2\text{O} = \text{H}^+ + \text{OH}^-$ ) that is necessary to maintain the correct balance between  $\text{H}^+$  and  $\text{OH}^-$  ions. The kinetic parameters for this reaction are taken from literature:  $k_f = 2.7 \times 10^{-5} \text{ s}^{-1}$  and  $k_b = 2.5 \times 10^8 \text{ m}^3 \text{ mol}^{-1} \text{ s}^{-1}$  [30,31].

## 4. Results and discussion

### 4.1. Oxygen solubility as a function of chloride concentration

The oxygen solubility in different electrolyte solutions has been a subject of numerous studies due to the great interest for geochemists, oceanographers and limnologists. Experimental data on oxygen solubility in NaCl electrolytes presented in literature are usually obtained using the Winkler method [32–35]. Analysis of the literature data shows that the linear Setschenow relationship that defines the oxygen solubility in an electrolyte  $c_{O_2}^{\text{el}}$  depending

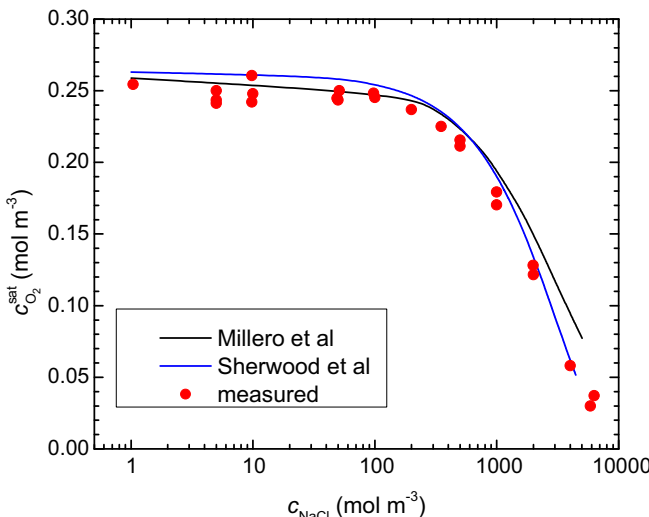


**Fig. 3.** Oxygen solubility as a function of NaCl concentration ( $p = 1 \text{ atm}$ ,  $T = 24\text{--}25^\circ\text{C}$ ). Measured  $\text{O}_2$  solubilities are approximated by Eq. (17). For comparison, data of Millero et al. [34] and Sherwood et al. [36] obtained by Winckler method are also presented.

on its concentration  $c_{\text{el}}$  and the oxygen solubility in distilled water  $c_{\text{O}_2^{\text{W}}}$

$$\ln \left( \frac{c_{\text{O}_2^{\text{W}}}}{c_{\text{O}_2^{\text{el}}} \cdot c_{\text{el}}} \right) = K \cdot c_{\text{el}}, \quad (16)$$

is valid only up to a salinity 20–30% [32]. Sherwood et al. [33] derived an empirical polynomial equation in order to describe the available experimental data on oxygen solubility in NaCl solutions up to 260%. Later, more elaborated thermodynamic models, based on the interaction of oxygen with electrolyte ions, were used to describe the oxygen solubility in pure water and different electrolytes in a wide range of concentrations, temperatures and pressures [34,35].

Also in corrosion applications it is very important to know the concentration of dissolved oxygen as its reduction rate often determines the rate of the corrosion process. In cyclic wet-dry conditions, the salt concentration can vary in a wide range due to evaporation/condensation of the electrolyte film. We dedicated to perform for the given laboratory conditions own oxygen solubility measurements using an amperometric technique described in Section 2.1. The results are presented in Fig. 3 and are in good agreement with the data of Millero et al. [34] and Sherwood et al. [36].

The experimentally measured dependency of oxygen solubility on chloride concentration was approximated by the following exponential function (all concentrations are in  $\text{mol m}^{-3}$ )

$$c_{\text{O}_2^{\text{sat}}} = 0.250 \cdot \exp(-3.03 \times 10^{-4} \cdot c_{\text{Cl}^-}). \quad (17)$$

This expression is used in the boundary condition (8) for all simulations.

#### 4.2. Potential distribution in the electrochemical cell

Potential distribution is very important for electrochemical measurements, especially in thin electrolyte layers. For that reason, the electrochemical cell used in this work was carefully designed in a way that the electrolyte potential would be distributed uniformly above the working electrode and in the area where the reference electrode is placed.

The MITReM allows calculation of the potential field in the electrochemical cell for a given electrolyte film thickness and salt concentration. Simulations were performed for three different

concentrations of NaCl: 5, 50 and 500  $\text{mol m}^{-3}$  (5, 50 and 500 mM) that are used for all measurements. In Fig. 4 the result of such calculation is presented for the most diluted 5 mM NaCl electrolyte. In addition, the electrolyte potential profiles extracted on the level of the working electrode surface for different electrolyte film thicknesses and salt concentrations are also shown. One can see that the maximal potential drop takes place in the thin electrolyte layer above the insulator while above the working electrode and in the vicinity of the counter electrode electrolyte potential is distributed uniformly. The simulations show that for thick layers ( $\delta_F > 500 \mu\text{m}$ ) of 5 mM NaCl potential drop in the electrolyte does not exceed 10 mV. For the most extreme case of 10  $\mu\text{m}$  layer of 5 mM NaCl solution electrolyte potential is about 0.21 V. Remark, however, that even with such a large ohmic drop, the imposed in simulations electrode potential ( $V - U$ ) is still well inside the oxygen limiting current region.

#### 4.3. Oxygen reduction under electrolyte films with constant thickness

In order to investigate the influence of the electrolyte thickness on the oxygen reduction, current transients were recorded on the Pt electrode covered by the NaCl electrolyte films of three different concentrations (5, 50 and 500 mM). Electrolyte film thickness  $\delta_F$  was different, but constant in time.

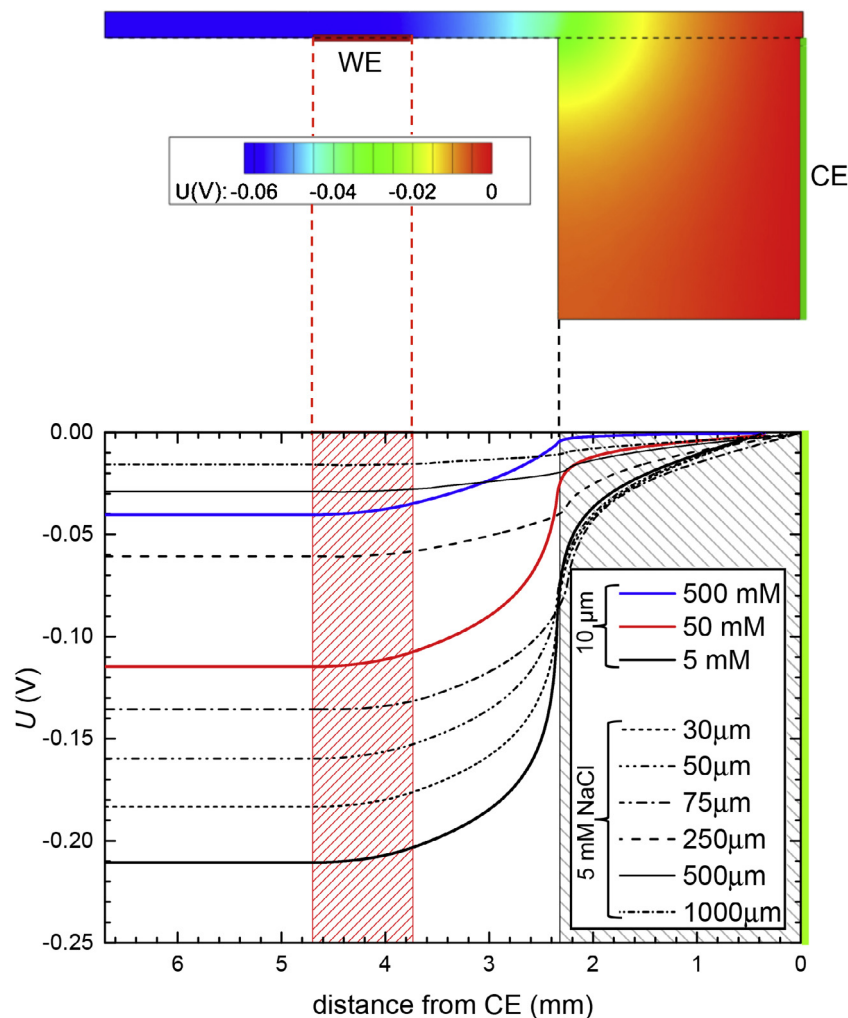
Examples of the experimental current transients are shown in Fig. 5 for 50 mM NaCl electrolyte. The transients have a shape that is typical for a diffusion-controlled processes: the current density drops very fast from its initial value and then reaches a constant value indicating the establishment of stationary oxygen diffusion. For thick films ( $\delta_F > 1 \mu\text{m}$ ) the steady state is reached within 1–2 min while for the thinner films it takes only about 10 s.

In order to validate the numerical MITRe model described in Section 3, time-dependent simulations were performed for the same conditions. The simulated current transients are compared in Fig. 5 with those obtained experimentally for the 50 mM NaCl solution. It can be seen that the simulated current evolution agrees well with the measured one for electrolyte film thicknesses  $\delta_F \geq 100 \mu\text{m}$ ; at lower thicknesses, the model overestimates the oxygen reduction current.

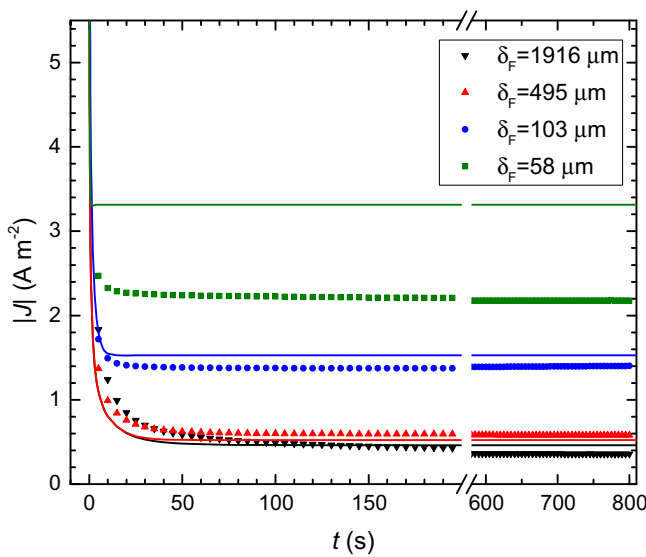
The steady state oxygen reduction current densities obtained for all three NaCl concentrations both in measurements and simulations are plotted in Fig. 6 versus the electrolyte film thickness. It can be seen that down to the thickness of  $\sim 500 \mu\text{m}$ , the oxygen reduction current is almost constant. With further decrease of the electrolyte film thickness the current rapidly increases. A similar behavior was observed e.g. by Zhang and Lyon for iron, copper and zinc in water [2], by Nishikata for platinum in NaCl [9], by Frankel [4] and Yamashita [11] for steel in NaCl and  $\text{Na}_2\text{SO}_4$  respectively. It is related to the diffusion control of the oxygen reduction reaction and the increased oxygen access to the electrode surface.

Fig. 7 gives more detailed comparison of the simulated and measured steady state oxygen current densities as it is expressed in  $J - 1/\delta_F$  coordinates. One can see that down to the film thickness 100–75  $\mu\text{m}$ , both experimental and simulated current densities obey Fick's law. For all three studied NaCl concentrations the current density is proportional to the reciprocal of the electrolyte film thickness (Fig. 7(a)). The slope of the  $J = f(1/\delta_F)$  dependencies is close to  $zFD_{\text{O}_2}c_{\text{O}_2^{\text{bulk}}}$ , the trends are consistent and the difference in the slopes between corresponding experimental and simulated curves does not exceed 3.5–11.5% (Table 2).

At lower layer thicknesses, both experimental and simulated current densities deviate from the linear Fick's behavior (Fig. 7(b)). Possible reasons of this deviation can be the increasing resistance (ohmic drop) between working and counter electrodes when the



**Fig. 4.** Electrolyte potential field for 250  $\mu\text{m}$  layer of 5 mM NaCl and potential profiles extracted along the dashed line for different concentrations and electrolyte film thicknesses



**Fig. 5.** Measured (symbols) and corresponding simulated (lines) current transients of oxygen reduction on Pt electrode covered by layers of 50 mM NaCl for given thicknesses.

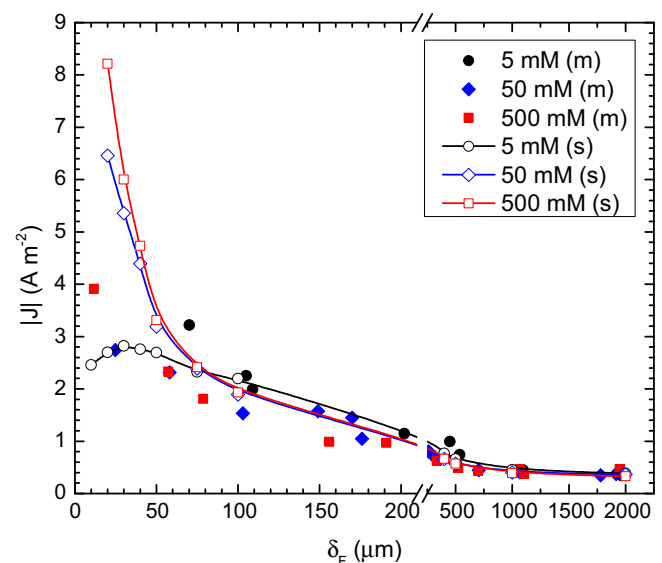


**Fig. 6.** Measured (m) and simulated (s) steady-state oxygen reduction current on Pt covered by the NaCl electrolyte layers of different thickness.

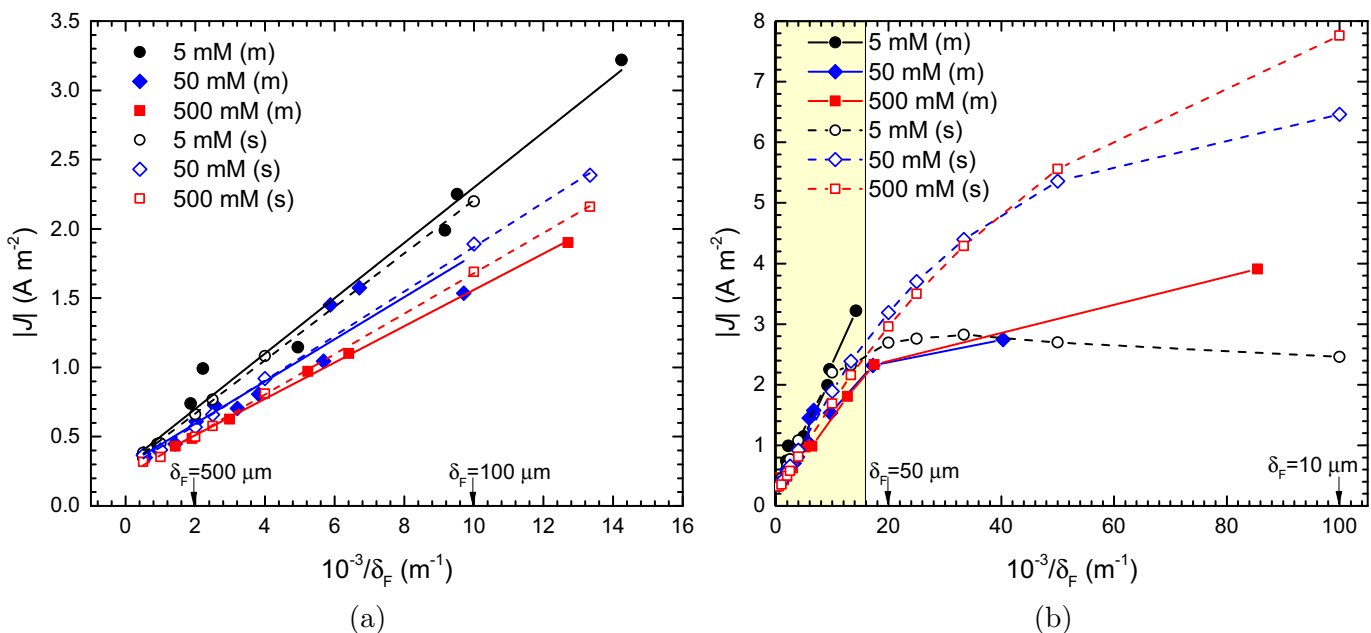


**Fig. 7.** Comparison of the measured (m) and simulated (s) steady-state currents of oxygen reduction (data from Fig. 6) in  $J - 1/\delta_F$  coordinates. The yellow area of the graph (b) corresponds to the range of the electrolyte film thicknesses where the Fick's law is valid (a). Slopes of the obtained  $J - 1/\delta_F$  dependences are listed in Table 2. (For interpretation of reference to color in this figure legend, the reader is referred to the web version of this article.)

electrolyte thickness goes down and/or diminished oxygen uptake from the air due to higher local  $\text{O}_2$  concentration (see Eq. (8)). Results of the simulations show that the ohmic drop becomes particularly relevant for the diluted 5 mM electrolyte and less pronounced for more concentrated solutions. Unfortunately in case of 5 mM NaCl it was not possible to verify the findings of the simulations as we could not obtain reproducible data for the thicknesses below 75  $\mu\text{m}$  due to the difficulties in maintaining uniform electrolyte layers with constant thickness and performing the electrochemical measurements in these conditions. From Fig. 7(b) one can also see that the simulated current densities for 50 mM and especially for 500 mM NaCl solutions are still overestimated, although the above mentioned effects are inherently taken into account by our MITRe model. This overestimation indicates that other phenomena, not considered in the model, may occur on the Pt surface in concentrated NaCl solutions. Reported by Stamenkovic et al. [37] poisoning of platinum surface by the adsorbed  $\text{Cl}^-$  ions that leads to a “strong inhibition of the oxygen reduction reaction” can be a possible explanation. The higher the NaCl concentration, the higher the amount of  $\text{Cl}_{\text{ads}}^-$ , and the lower oxygen reduction rate should be measured. Another possible reason can be increasing contribution into total current of two-electron oxygen reduction mechanism, which seems to be facilitated in highly alkaline media [28,29] and by anion adsorption on Pt surface [27].

A major advantage of the MITReM simulations is that they provide the distributions of all species concentrations in the system. While most of these concentrations are not readily accessible by experimental techniques, pH maps can be measured using

ion-selective microelectrodes. In order to investigate the influence of the electrolyte film thickness on the pH distribution, stationary simulations were performed. The simulations presented in Fig. 8a for 50 mM NaCl electrolyte indicate that pH above the electrode increases substantially (from 10.7 to 12.4) and that the area of high pH becomes wider when the electrolyte film thickness goes down from 2 mm to 100  $\mu\text{m}$ . Increase of pH for thinner electrolyte films was also found in Ref. [5]. pH mapping performed for the same conditions in order to calibrate the model show similar trends, however the measured pH in the electrode area is 0.5–1.0 units lower than the simulated one, Fig. 8b. This difference can be related to the fact that stationary simulations give the equilibrium result at infinite time, while during the measurements the equilibrium might have not been reached yet, especially in the presence of  $\text{CO}_2$ , which acts as a buffer.

#### 4.4. Oxygen reduction under evaporating electrolyte films

During the drying of an electrolyte film, oxygen reduction is influenced by two phenomena, which have the opposite effects. On the one hand, reducing electrolyte layer allows better oxygen access to the electrode surface leading to an increase in the recorded current density. On the other hand, the salt concentration increases dramatically during evaporation which reduces the oxygen solubility. As a result, oxygen current transients recorded under the evaporating electrolyte layers are usually more complex than those for the constant film thicknesses.

Measurements of the oxygen reduction current were performed for the same initial concentrations of NaCl as for the experiments described in Section 4.3, namely 5, 50 and 500 mM. For each concentration, at least two different initial electrolyte layer thicknesses were used in order to investigate the role of both factors.

Typical current transient is shown in Fig. 9(a) for the case of 50 mM NaCl electrolyte evaporating from 600  $\mu\text{m}$  till drying. In time, the recorded current density first increases rapidly due to the increased oxygen access, goes through a maximum and then decreases. The shape of the recorded current transients is similar

**Table 2**

Experimental and simulated slopes of the  $J - 1/\delta_F$  dependences for different NaCl concentrations (data from Fig. 7(a))

NaCl (mol $\text{m}^{-3}$ )	Slope $\times 10^4$ , $\text{A m}^{-1}$		$zFD_{\text{O}_2} c_{\text{O}_2}^{\text{bulk}} \times 10^4$ $\text{A m}^{-1}$
	Experimental	Simulated	
5	2.00	1.96	1.89
50	1.52	1.61	1.86
500	1.31	1.46	1.58

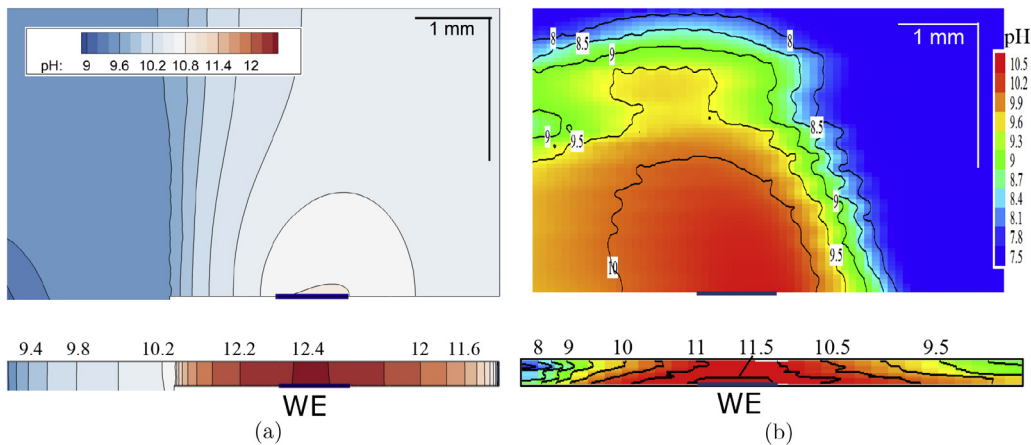


**Fig. 8.** Simulated (a) and measured (b) pH distributions in 50 mM NaCl electrolyte films of 2 mm and 100  $\mu\text{m}$  thickness.

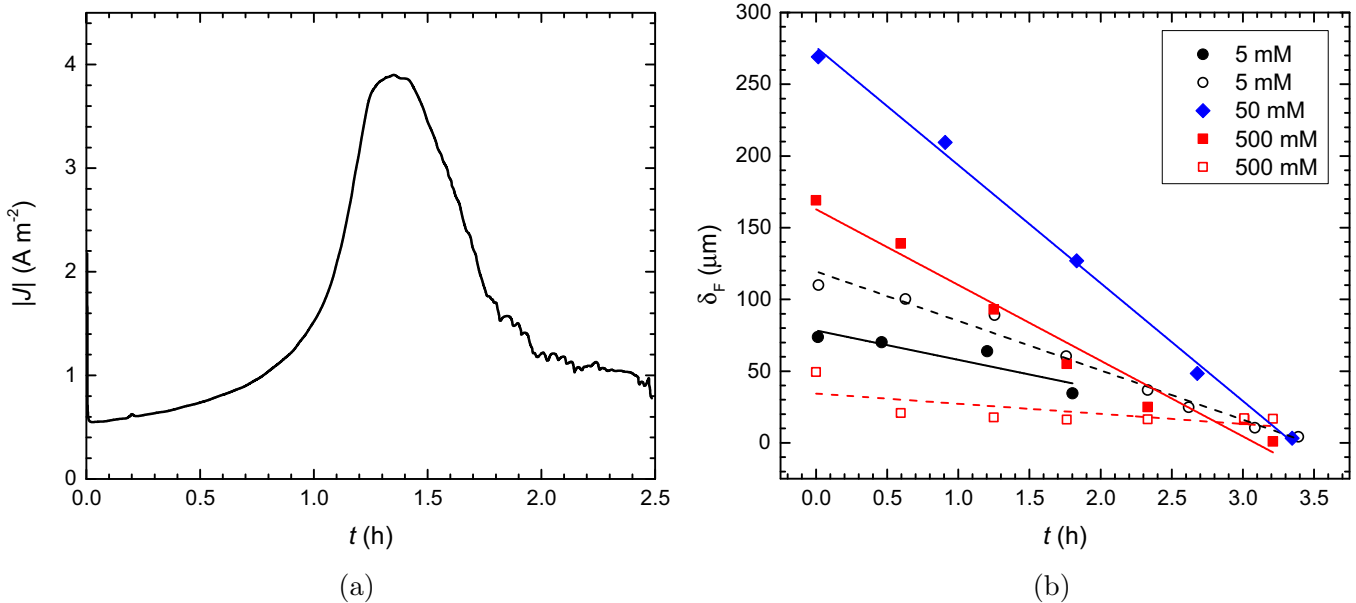


**Fig. 9.** Typical current transient for oxygen reduction on Pt electrode covered by the evaporating 50 mM NaCl electrolyte layer (a) and the electrolyte film thickness as a function of time for different concentrations of NaCl (b). Calculated evaporation rates are listed in Table 3.

to the ones presented in the work of Stratmann and Streckel [38], Mansfeld and Tsai [39] and Tomashov [40].

During the evaporation process, the electrolyte film thickness was periodically measured using the needle and the optical system described in Section 2.2. That allowed to estimate the evaporation rates for different initial conditions. Fig. 9(b) shows the obtained results. It was found that the evaporation rate depends not only on the initial NaCl concentration but, even more strongly, on the initial electrolyte film thickness. Thicker films evaporate apparently much faster than the thinner ones (see Table 3). Similar effect was noticed by other authors [4]. This effect can be attributed to a better mixing

in thick layers that leads to a higher air-electrolyte temperature difference and, as a consequence, to a higher evaporation rate.

The simulations of oxygen reduction under evaporating films were performed in a simplified manner: using 1D geometry and assuming a constant evaporation rate (corresponding to the chosen initial NaCl concentration and electrolyte film thickness, namely 110  $\mu\text{m}$  for 5 mM NaCl, 270  $\mu\text{m}$  for 50 mM NaCl and 170  $\mu\text{m}$  for 500 mM NaCl). Since during the measurements the evaporation rate is not constant and changes continuously depending on the layer thickness and salt concentration, a direct comparison of the simulated current transients with the experimental ones was not possible. However, using the data of the Table 3 we could estimate the evolution of the electrolyte film thickness for each experimental current transient and compare the simulated and measured current densities for the same electrolyte film thicknesses.

The results of this comparison are shown in Fig. 10. One can see that the simulations are able to reproduce the oxygen current density evolution for 500 mM NaCl, with the maximum oxygen current density at about 30  $\mu\text{m}$ , in the full range of the film thicknesses (down to 2–3  $\mu\text{m}$ ). At the same time, for 5 and 50 mM NaCl a good agreement between simulations and measurements

**Table 3**

Evaporation rate calculated for different initial NaCl electrolyte film thicknesses and concentrations (data from Fig. 9)

$c_{\text{NaCl}}$ , mol $\text{m}^{-3}$	$\delta_F^{\text{initial}}$ , $\mu\text{m}$	$v_{\text{evap}}$ , $\mu\text{m h}^{-1}$
5	75	20.5
5	110	34.5
50	270	82.2
500	30	3.6
500	170	63.8

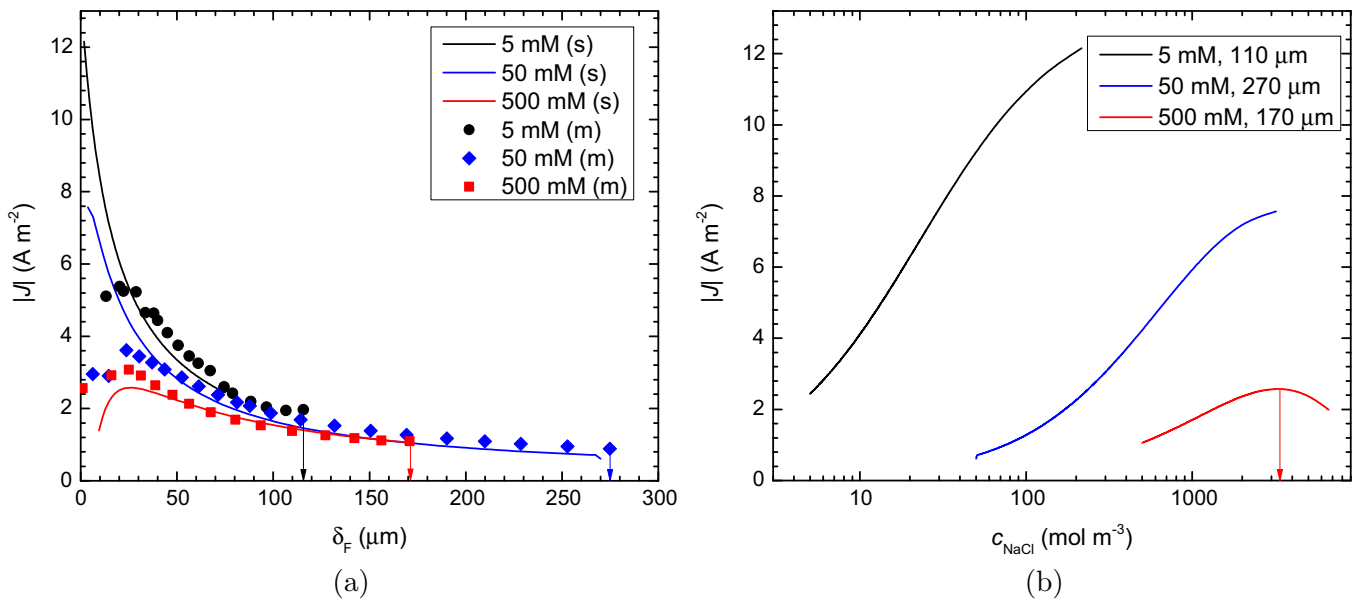


**Fig. 10.** Comparison of the measured (m) and simulated (s) dependencies of oxygen reduction current on the evaporating electrolyte layer thickness (a) and the simulated oxygen reduction current as a function of NaCl concentration for different initial conditions (b).

is observed only for electrolyte layer thicknesses  $\delta_F > 25 \mu\text{m}$ . While the model predicts a constant increase of the oxygen current density with decrease of the electrolyte film thickness down to 1 μm, the measured current reaches its maximum at 10–20 μm and then decreases.

This can be explained as follows. As mentioned before, there are two factors that influence the oxygen reduction limiting current under evaporating electrolyte films – the electrolyte film thickness  $\delta_F$  and the oxygen saturation concentration  $c_{\text{O}_2}^{\text{sat}}$ , which depends on chloride concentration according to Eq. (17):

$$J_{\text{O}_2}^{\text{lim}} = zFD_{\text{O}_2}c_{\text{O}_2}^{\text{sat}}(c_{\text{Cl}^-}) \times \frac{1}{\delta_F}. \quad (18)$$

Taking into account that chloride concentration in turn changes with the electrolyte film thickness

$$c_{\text{Cl}^-} = \frac{c_{\text{Cl}^-}^{\text{init}}\delta^{\text{init}}}{\delta_F}, \quad (19)$$

one can derive an expression for the oxygen limiting current, which is a function of the electrolyte film thickness only:

$$J_{\text{O}_2}^{\text{lim}} = zFD_{\text{O}_2}c_{\text{O}_2}^{\text{sat},0} \exp\left(-\frac{a \cdot c_{\text{Cl}^-}^{\text{init}}\delta^{\text{init}}}{\delta_F}\right) \times \frac{1}{\delta_F}, \quad (20)$$

where  $c_{\text{O}_2}^{\text{sat},0} = 0.25 \text{ mol m}^{-3}$  and  $a = 3.03 \times 10^{-4} \text{ m}^3 \text{ mol}^{-1}$  (see Eq. (17)). The critical film thickness that corresponds to the maximum current density can be obtained by taking a derivative of Eq. (20) with respect to  $\delta_F$  and equating it to zero. One can see that it depends on the initial electrolyte film thickness and salt concentration:

$$\frac{\partial J_{\text{O}_2}^{\text{lim}}}{\partial \delta_F} = 0 \quad \text{at} \quad \delta_F^{\text{crit}} = ac_{\text{Cl}^-}^{\text{init}}\delta^{\text{init}}. \quad (21)$$

Critical chloride concentration corresponding to the  $\delta_F^{\text{crit}}$  can be found by substitution of Eq. (21) into Eq. (19):

$$c_{\text{Cl}^-}^{\text{crit}} = \frac{c_{\text{Cl}^-}^{\text{init}}\delta^{\text{init}}}{ac_{\text{Cl}^-}^{\text{init}}\delta^{\text{init}}} = \frac{1}{a} = \frac{1}{3.03 \times 10^{-4}} = 3300 \text{ mol m}^{-3}. \quad (22)$$

Remark, that  $c_{\text{Cl}^-}^{\text{crit}}$  is independent of the initial conditions and is determined only by the change of oxygen solubility as a function of chloride. When chloride concentration is below the critical value, the enhanced oxygen access to the electrode surface plays the major role in the increase of limiting current when the electrolyte thickness goes down. Above the critical concentration, the effect of a lesser oxygen solubility becomes relevant.

For the most concentrated solution of 500 mM NaCl with initial thickness  $\delta^{\text{init}} = 270 \mu\text{m}$ , the critical salt concentration is reached at about 26 μm resulting in the current maximum. If the initial thickness and salt concentrations are relatively low, like for 5 and 50 mM NaCl, the critical salt concentration cannot be reached during the evaporation process. As a consequence the simulated oxygen reduction currents for these concentrations steadily increase with decreasing electrolyte layer thickness (see Fig. 10(b)) while in practice the current maximum is observed even for these concentrations. A possible reason for such a discrepancy can be the fact that the model in its present state does not take into account for example the chloride adsorption on the Pt surface discussed in the Section 4.3 and reduced ion mobilities in concentrated solutions. Both these effects can lead to a situation when cathodic current reaches its maximum at a chloride concentration lower than the critical value calculated here. However, when making an abstraction from these effects, we believe that the developed model is capable to predict correctly oxygen reduction behavior in chloride electrolytes.

## 5. Conclusions

In view of quantifying corrosion under thin electrolyte layers, in this article we present the results of electrochemical measurements and numerical simulations of the oxygen reduction on a platinum electrode covered by NaCl electrolyte layers of constant and changing in time thickness and concentration. In order to provide the input information for the numerical model, dedicated measurements of the oxygen solubility in sodium chloride solutions for a wide range of salt concentrations were performed using an amperometric technique. The results of these measurements are in a good agreement with the literature data obtained by the standard Winkler method. For the model calibration, current transients and pH maps were recorded during cathodic polarization of Pt electrode

covered by the NaCl layer of varying thickness and concentration. The results of the measurements show that if the electrolyte layer thickness  $\delta_F$  is not changing in time, the oxygen reduction current is proportional to  $1/\delta_F$  for the films thicknesses down to 100–75  $\mu\text{m}$ ; with further decrease of the electrolyte film thickness, a deviation from Fick's law takes place. In the evaporating electrolyte films, oxygen reduction current density reaches a maximum at  $\sim 25 \mu\text{m}$  and then decreases.

The developed mechanistic MITRe model considers the chloride concentration dependent oxygen uptake at the air/electrolyte interface, its transport through the solution and subsequent discharge on the platinum electrode. Transport of other relevant species due to diffusion, migration and micro-convection ( $\text{Na}^+$ ,  $\text{Cl}^-$ ,  $\text{H}^+$ ,  $\text{OH}^-$ ), and water dissociation reaction are also taken into account. The model provides current transients for constant and time-varying conditions (electrolyte thickness and chloride concentration) as well as the distribution of species in the electrolyte.

Comparison with the measurements, which becomes quite difficult for very thin electrolyte layers, shows that the oxygen reduction is correctly modeled down to  $\sim 75 \mu\text{m}$  in the case of the constant NaCl concentration and down to  $\sim 50 \mu\text{m}$  for the evaporating electrolyte. The current density is determined by the oxygen uptake and transport on the one hand and changes in oxygen solubility on the other hand. The latter becomes relevant starting from the NaCl concentration  $\sim 3.3 \text{ mol L}^{-1}$ . For thinner films, the model overestimates the oxygen reduction current. It is believed that this overestimation might be due a possible poisoning of the Pt surface by the adsorbed chloride ions, transition from four-electron to two-electron oxygen reduction reaction and/or the reduced ion mobility in concentrated solutions – the phenomena currently not considered in the model. Including these effects would result in further improvement of the model, however, even in the present stage it predicts correctly the main features of oxygen reduction in thin electrolyte films.

## Acknowledgment

This work was carried out in the frame of the RFCS project AtCorAS “Modeling of atmospheric corrosion of steel protected by aluminum based alloys, applied by hot dip processing” (RFSR-CT-2011-00015).

## References

- [1] N. Tomashov, Development of the electrochemical theory of metallic corrosion, *Corrosion* 20 (1) (1964) 7t–14t.
- [2] X. Zhang, E. Valeriote, Galvanic protection of steel and galvanic corrosion of zinc under thin layer electrolytes, *Corros. Sci.* 34 (1993) 1957–1972.
- [3] M. Stratmann, H. Streckel, On the atmospheric corrosion of metals which are covered with thin electrolyte layers. Verification of the experimental technique, *Corros. Sci.* 30 (6â7) (1990) 681–696.
- [4] G. Frankel, M. Stratmann, M. Rohwerder, A. Michalik, B. Maier, J. Dora, M. Wicinski, Potential control under thin aqueous layers using a Kelvin Probe, *Corros. Sci.* 49 (2007) 2021–2036.
- [5] M. Keddam, A. Hugot-Le-Goff, H. Takenouti, D. Thierry, M. Arevalo, The influence of a thin electrolyte layer on the corrosion process on zinc in chloride-containing solutions, *Corros. Sci.* 33 (8) (1992) 1243–1252.
- [6] A. Nishikata, Y. Ichihara, Y. Hayashi, T. Tsuru, Electrochemical impedance spectroscopy of metals covered with a thin electrolyte layer, *Electrochim. Acta* 41 (7–8) (1996) 1057–1062.
- [7] E. Remita, E. Sutter, B. Tribollet, F. Ropital, X. Longaygue, C. Taravel-Condat, N. Desamais, A thin layer cell adapted for corrosion studies in confined aqueous environments, *Electrochim. Acta* 52 (2007) 7715–7723.
- [8] G. El-Mahdy, A. Nishikata, T. Tsuru, AC impedance study on corrosion of 55%Al-Zn alloy-coated steel under thin electrolyte layers, *Corros. Sci.* 42 (2000) 1509–1521.
- [9] A. Nishikata, Y. Ichihara, Y. Hayashi, T. Tsuru, Influence of electrolyte layer thickness and pH on the initial stage of the atmospheric corrosion of iron, *J. Electrochim. Soc.* 144 (4) (1997) 1244–1252.
- [10] Y. Cheng, Z. Zhang, F. Cao, J. Li, J. Zhang, J. Wang, C. Cao, A study of the corrosion of aluminum alloy 2024-T3 under thin electrolyte layers, *Corros. Sci.* 46 (2004) 1649–1667.
- [11] M. Yamashita, H. Nagano, R. Oriani, Dependence of corrosion potential and corrosion rate of a low-alloy steel upon depth of aqueous solution, *Corros. Sci.* 40 (9) (1998) 1447–1453.
- [12] E. Dubuisson, P. Lavie, F. Dalard, J.-P. Caire, S. Szunerits, Corrosion of galvanized steel under an electrolytic drop, *Corros. Sci.* 49 (2) (2007) 910–919.
- [13] S. Zhang, S. Lyon, The electrochemistry of iron, zinc and copper in thin layer electrolytes, *Corros. Sci.* 35 (1–4) (1993) 713–718.
- [14] M.S. Venkatraman, I.S. Cole, B. Emmanuel, Model for corrosion of metals covered with thin electrolyte layers: Pseudo-steady state diffusion of oxygen, *Electrochim. Acta* 56 (20) (2011) 7171–7179.
- [15] S. Palani, T. Hack, J. Deconinck, H. Lohner, Validation of predictive model for galvanic corrosion under thin electrolyte layers: an application to aluminium 2024-CFRP material, *Corros. Sci.* 78 (2014) 89–100.
- [16] F. Thébault, B. Vuillemin, R. Oltra, C. Allely, K. Ogle, Modeling bimetallic corrosion under thin electrolyte films, *Corros. Sci.* 53 (1) (2011) 201–207.
- [17] A. van Stroe, L. Jansen, Determination of the diffusion coefficient of oxygen in sodium chloride solutions with a transient pulse technique, *Anal. Chim. Acta* 279 (1993) 213–219.
- [18] J. Kestin, H.E. Khalifa, R. Correia, Tables of the dinamic and kinematic viscosity of aqueous NaCl solutions in the temperature range 20–150 °C and the pressure range 0.1–35 MPa, *J. Phys. Chem. Ref. Data* 10 (1981) 71–87.
- [19] A. Bastos, O. Karavai, M. Zheludkevich, K. Yasakau, M. Ferreira, Localised measurements of pH and dissolved oxygen as complements to SVET in the investigation of corrosion at defects in coated aluminum alloy, *Electroanalysis* 500 (2010) 2009–2016.
- [20] V. Levich, *Physicochemical Hydrodynamics*, Prentice-Hall, Englewood Cliffs, NJ, 1962.
- [21] C. Amatore, S. Szunerits, L. Thouin, J.-S. Warkocz, The real meaning of Nernst's steady diffusion layer concept under non-forced hydrodynamic conditions. A simple model based on Levich's seminal view of convection's steady diffusion layer concept under non-forced hydrodynamic conditions. a simple model based on levich's seminal view of convection, *J. Electroanal. Chem.* 500 (1–2) (2001) 62–70.
- [22] O. Dolgikh, A. Demeter, A. Bastos, V. Topa, J. Deconinck, A practical way to model convection in non-agitated electrolytes, *Electrochim. Commun.* 37 (2013) 20–23.
- [23] J. Sethian, *Level Set methods and Fast Marching Methods: Evolving Interfaces in Computational Geometry, Fluid Mechanics, Computer Vision and Materials Science*, Cambridge University Press, 1999.
- [24] T. Wuilaut, *Algorithmic developments for a multiphysics framework (Ph.D. thesis)*, Université Libre de Bruxelles, von Karman Institute for Fluid Dynamics, 2008.
- [25] H. Davis, G. Crandall, The role of the liquid stationary film in batch absorptions of gases. I. Absorption's involving no irreversible chemical reactions, *J. Am. Chem. Soc.* 52 (1930) 3757–3768.
- [26] J. Hoare, *The Electrochemistry of Oxygen*, John Wiley, London, and Interscience, New York, 1968.
- [27] A. Damjanovic, V. Brusic, Electrode kinetics of oxygen reduction on oxide-free platinum electrodes, *Electrochim. Acta* 12 (1967) 615–628.
- [28] K.-L. Hsueh, E. Gonzalez, S. Srinivasan, Electrolyte effects on oxygen reduction kinetics at platinum: a rotating ring-disc electrode analysis, *Electrochim. Acta* 28 (5) (1983) 691–697.
- [29] N. Markovic, T. Schmidt, V. Stamenkovic, P. Ross, Oxygen reduction reaction on Pt and Pt bimetallic surfaces: a selective review, *Fuel Cells* 1 (2) (2001) 105–116.
- [30] *Handbook of Chemistry and Physics*, 76th ed., CRC Press, 1995.
- [31] W. Stumm, J. Morgan, *Aquatic Chemistry: Chemical Equilibria and Rates in Natural Waters*, John Wiley & Sons Inc., 1996.
- [32] M. Hitchman, *Measurements of Dissolved Oxygen*, Vol. 49 of *Chemical Analytical Chemistry and its Applications*, John Wiley & Sons Inc., 1978.
- [33] J. Sherwood, F. Stagnitti, M. Kokkinn, W. Williams, Dissolved oxygen concentrations in hypersaline waters, *Limnol. Oceanogr.* 36 (2) (1991) 235–250.
- [34] F. Millero, F. Huang, A. Laferiere, Solubility of oxygen in the major sea salts as a function of concentration and temperature, *Mar. Chem.* 78 (4) (2002) 217–230.
- [35] M. Geng, Z. Duan, Prediction of oxygen solubility in pure water and brines up to high temperatures and pressures, *Geochim. Cosmochim. Acta* 74 (2010) 5631–5640.
- [36] J. Sherwood, F. Stagnitti, M. Kokkinn, W. Williams, A standard table for predicting equilibrium dissolved oxygen concentrations in salt lakes dominated by sodium chloride, *Int. J. Salt Lake Res.* 1 (1992) 1–6.
- [37] V. Stamenkovic, N. Markovic, P. Ross, Structure-relationships in electrocatalysis: oxygen reduction and hydrogen oxidation reaction on Pt(111) and Pt(100) in solutions containing chloride ions, *J. Electroanal. Chem.* 500 (2001) 44–51.
- [38] M. Stratmann, H. Streckel, On the atmospheric corrosion of metals which are covered with thin electrolyte layers – II. Experimental results, *Corros. Sci.* 30 (6–7) (1990) 697–714.
- [39] F. Mansfeld, S. Tsai, Laboratory studies of atmospheric corrosion. I. Weight loss and electrochemical measurements, *Corros. Sci.* 20 (1980) 853–872.
- [40] N. Tomashov, *Theory of Corrosion and Protection of Metals*, MacMillan Company, 1966.
- [41] J. Newman, K. Thomas-Aleya, *Electrochemical Systems*, 3rd ed., John Wiley & Sons Inc., 2004.